

Phantom-Based Ultrasound-ECG Deep Learning Framework for Prospective Cardiac Computed Tomography

Shambavi Ganesh*, Brooks D. Lindsey, Srini Tridandapani, and Pamela T. Bhatti

Abstract— Objective: We present the first multimodal deep learning framework combining ultrasound (US) and electrocardiography (ECG) data to predict cardiac quiescent periods (QPs) for optimized computed tomography angiography gating (CTA). **Methods:** The framework integrates a 3D convolutional neural network (CNN) for US data and an artificial neural network (ANN) for ECG data. A dynamic heart motion phantom, replicating diverse cardiac conditions, including arrhythmias, was used to validate the framework. Performance was assessed across varying QP lengths, cardiac segments, and motions to simulate real-world conditions. **Results:** The multimodal US-ECG 3D CNN-ANN framework demonstrated improved QP prediction accuracy compared to single-modality ECG-only gating, achieving 96.87% accuracy compared to 85.56%, including scenarios involving arrhythmic conditions. Notably, the framework shows higher accuracy for longer QP durations (100 ms - 200 ms) compared to shorter durations (<100 ms), while still outperforming single-modality methods, which often fail to detect shorter quiescent phases, especially in arrhythmic cases. Consistently outperforming single-modality approaches, it achieves reliable QP prediction across cardiac regions, including the whole phantom, interventricular septum, and cardiac wall regions. Analysis of QP prediction accuracy across cardiac segments demonstrated an average accuracy of 92% in clinically relevant echocardiographic views, highlighting the framework's robustness. **Conclusion:** Combining US and ECG data using a multimodal framework improves QP prediction accuracy under variable cardiac motion, particularly in arrhythmic conditions. **Significance:** Since even small errors in cardiac CTA can result in non-diagnostic scans, the potential benefits of multimodal gating may improve diagnostic scan rates in patients with high and variable heart rates and arrhythmias.

Index Terms—Cardiac Quiescence Prediction, Multimodal Gating Framework, Ultrasound, Electrocardiography, Deep Learning, CNN, ANN, Computed Tomography Angiography Gating, Dynamic Heart Motion Phantom

This work was supported by the U.S. National Science Foundation under Grant 2122299.

S. Tridandapani is with the Department of Radiology, University of Alabama, Birmingham, AL, USA. B. D. Lindsey is with the Wallace H. Coulter Department of Biomedical Engineering, Georgia Institute of Technology, Atlanta, GA, USA. *S. Ganesh and P. T. Bhatti are with the School of Electrical and Computer Engineering, Georgia Institute of Technology, Atlanta, GA, USA (correspondence email: shambavi.ganesh@gatech.edu).

I. INTRODUCTION

ACCORDING to the World Health Organization (WHO), cardiovascular disease (CVD) claims over 17.9 million lives annually [1]. CVD encompasses a wide category of heart and blood vessel disorders, affecting people across all demographics. Coronary artery disease (CAD), a type of CVD, involves stenosis or occlusion of coronary arteries, potentially leading to angina, myocardial infarction, or sudden cardiac death [2]. Cardiac arrhythmia, affecting 1–1.5% of the global population, disrupts normal heart rhythm [3]. Notably, 0.2–5% of CAD patients also have arrhythmias, representing a global population of approximately 0.5 to >12 million [4,5]. Accurate diagnosis and timely intervention, such as percutaneous coronary intervention (PCI), are critical in reducing major adverse cardiac events [6].

The gold standard for evaluating coronary artery structure is catheter coronary angiography (CCA), an invasive procedure performed in the cardiac catheterization lab that requires an intra-arterial contrast agent to visualize any stenoses [4,5,7]. However, because CCA is invasive, costly, and can have complications [5], cardiac computed tomography angiography (CTA) is used as an initial gatekeeper to determine which patients should be sent to the cardiac catheterization lab for further testing [8,9].

CTA utilizes X-ray computed tomography and an intravenous contrast agent to acquire non-invasive, high-resolution, 3D images of coronary arteries [10]. CTA is less invasive, faster, and less expensive than CCA, thus according to the 2021 Chest Pain Guidelines issued by the American College of Cardiology/American Heart Association, CTA may be used to rule out the need for cardiac catheterization in patients with low to intermediate risk for major adverse cardiac events such as myocardial infarction (MI) [11,12]. A CTA-guided strategy can reduce costs by 57% compared to direct CCA referral (\$1,183 vs. \$2,755) per patient, with additional savings from avoiding CCAs [13]. If at least 0.5 million patients have both CAD and arrhythmia [4,5], and 36% of CCAs could be avoided [13], at a minimum potential healthcare savings would be approximately \$212 million, based on an average cost reduction of \$1,183 per case with a CTA-guided approach.

Because CTA has limited temporal resolution, gating acquisition of imaging data is critical. Accurately detecting

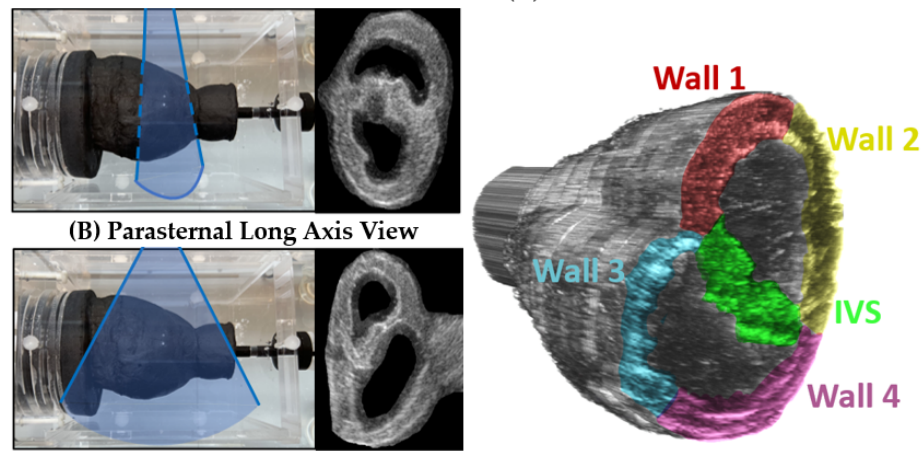


Fig. 1. Two DHP-based views used for acquiring data. (A) (Left-Right) Using a Philips P4-1 transducer, imaging data is acquired in the parasternal long axis (PSLA) view. The right image shows the corresponding B-mode image. (B) (Left-Right) Upon rotation of the transducer by 90 degrees, the parasternal short axis (PSSA) view is acquired. The image on the right is the corresponding B-mode image. (C) 3D rendering of multiple slices of acquired B-mode ultrasound imaging data using a computer-controlled motion stage in the elevation direction. The investigated wall segments and the IVS are indicated in color.

the quiescent period (QP) of the heart can allow the acquisition of diagnostic-quality scans while reducing the radiation dose to the patient. Clinical CT systems typically use electrocardiography (ECG) gating, with the technologist selecting a temporal window that includes the cardiac QP (i.e. the time when cardiac motion is at a minimum) [14]. However, while increasing the duration of the window increases the likelihood of acquiring a diagnostic-quality scan, this also increases the radiation dose to the patient [15]. Gating can be implemented either prospectively or retrospectively [16]. Prospective gating relies on a cardiac signal-based trigger, such as an ECG signal, which results in CTA data being selectively acquired at predetermined quiescent period times within a cardiac cycle. Conversely, retrospective gating acquires CTA data continuously throughout the cardiac cycle, with optimal phases selected later during image reconstruction to produce the best images.

Two main approaches have been investigated for QP detection. Previous studies have demonstrated echocardiography to be an effective tool for the detection of cardiac quiescence [15-19]. In addition, seismocardiography, which measures cardiac-generated vibrations on the chest wall, has also been shown to accurately identify quiescent phases, offering another non-invasive alternative for optimizing cardiac imaging [20]. One challenge to the use of ultrasound (US) for gating CTA acquisition was previously limited due to prominent streak artifacts caused by radiopaque materials in commercial US transducers, such as piezoelectric elements and dense acoustic backing [21]. As a result, US data was traditionally used to establish baseline cardiac quiescence [16,18], but not integrated into the CT acquisition workflow. Recently, the development of a CT-compatible transducer array enabled in vivo imaging of the interventricular septum (IVS) [22,23], paving the way for ultrasound to be utilized in CTA gating.

This work develops and evaluates a deep learning-based multimodal gating framework that integrates US and ECG for predicting cardiac quiescence. A 3D convolutional neural network (CNN) is implemented to process combined US and

ECG data. It is compared with the ECG-based artificial neural network (ANN) architecture previously established by our group [24]. The framework is tested using data from a dynamic heart motion phantom (DHP) [25], which provides a controlled, programmable environment to replicate cardiac motion with known ground truth, including arrhythmic scenarios (Fig. 1). The anthropomorphic DHP offers repeatable cardiac motion, enabling validation and refinement of gating algorithms prior to clinical testing. Establishing baseline performance on phantom data allows for accurate assessment of the developed approach and identification of limitations across both healthy and arrhythmic cardiac cycles, as an important step for clinical translation.

The goal of this work is to:

- 1) Develop cardiac quiescence prediction using a cardiac phantom at higher heart rates (>60 bpm) and under arrhythmic conditions.
- 2) Identify the spatial locations across the cardiac phantom best suited for the prediction of quiescent periods. Specifically, the performance of the prediction algorithm is compared across various 2D segments of the cardiac phantom, including the ventricular walls, the interventricular septum (IVS) and the entire phantom, as illustrated in Fig. 1(C).
- 3) Finally, for the entire phantom, the predictive power of the proposed algorithm is investigated across the various temporal segments within a cardiac cycle.

The remainder of the paper is organized as follows. In Section II, we provide a comprehensive overview of the methodology employed in this study, including the experimental design, data acquisition techniques, and analytical approaches utilized. In Section III we present the results of the cardiac quiescence prediction in the phantom detailed. The discussion and conclusion are presented in sections IV and V, respectively.

II. METHODS

This section outlines the novel algorithms developed to predict cardiac quiescence using both ECG and ultrasound (US) data, along with their validation. Section (A) describes data acquisition from a commercial dynamic heart phantom (DHP) and the quiescence prediction algorithm. Section (B) details the validation process, with results provided in the Appendix. Validation involved assessing algorithm performance across different physical cross-sections of the DHP using incomplete US acquisitions from partial cardiac cycles for a thorough evaluation. The deep learning framework was trained and tested on a beat-by-beat basis, using both US and ECG data as inputs to predict cardiac quiescence across DHP segments. The availability of known ground truth quiescence in the DHP enabled precise evaluation of the developed prediction methods.

A. Data Acquisition using a Dynamic Heart Phantom

The dynamic heart motion phantom (DHP-01, Shelley Medical Imaging Technologies, London, ON, Canada) is a commercial anthropomorphic phantom designed for multimodal imaging of cardiac motion [25]. It contains two ventricle-like chambers, with volumes of 67 mL for the left chamber and 77 mL for the right chamber (Fig. 1). The motion of the DHP is controlled using Visual Show Automation (VSA Hobbyist) software (Fig. 2), enabling precise replication of synthetic cardiac motion representative of physiological conditions. This controlled experimental framework facilitates the development and validation of advanced cardiac gating algorithms.

Asynchronous cardiac-motion-based signals were acquired from the phantom to predict cardiac QPs. These signals were also used to validate the accuracy of the predicted QPs. The experimental setup (Fig. 3) enabled the acquisition of data from three distinct modalities: optical imaging, US imaging, and ECG. Each modality provided unique insights into cardiac motion dynamics. First, optical imaging (Canon EOS 60D camera, Tokyo, Japan) enabled high-resolution visualization of the DHP motion and was used to establish the ground truth. Ultrasound data were acquired using a cardiac phased array transducer (P4-1, Philips, Bothell, WA, USA) connected to a research system (Verasonics Vantage 256, Kirkland, WA, USA). Finally, the passive ECG signal was artificially

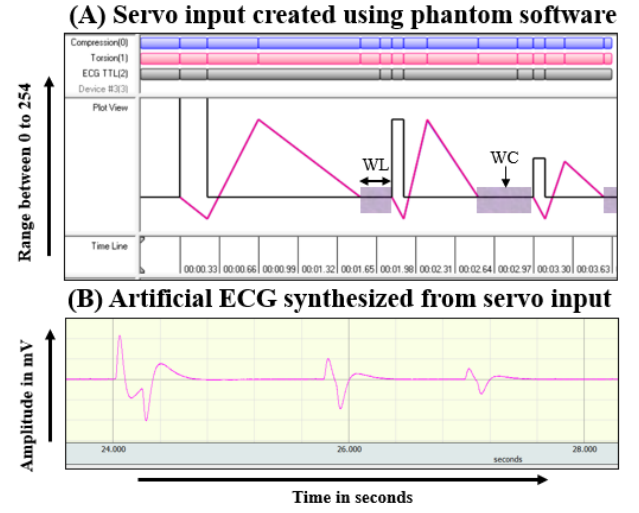


Fig. 2. Screenshot of the Visual Show Automation (VSA) software. (A) The event view window illustrates three signals utilized to create the phantom motion utilized in the experiments: Compression (blue), Torsion (red), and ECG (gray) signals. The length of the bars corresponds to the time duration of DHP motion. The Plot View of the DHP (black) depicts the magnitude of the artificial ECG signal. (B) An artificial ECG is synthesized from this plot.

generated. The ECG-like signal (Fig. 3(C)) was output by a commercial passive ECG adapter, which is part of the dynamic heart motion phantom (PI-ECG1, Shelley Medical Imaging Technologies, ON, Canada). This synthetic ECG signal was created by averaging input motion control signals fed into the DHP.

Additionally, two imaging views were obtained from the phantom, as shown in Fig. 1. The parasternal long-axis (PSLA) and parasternal short-axis (PSSA) views, as depicted in Fig. 1(A), are standard echocardiographic imaging views used in clinical practice [26]. Front and top views of the setup are showcased in Fig. A1, of the Appendix.

Experiments were designed to simulate a range of cardiac motion scenarios using data from optical, US, and ECG modalities acquired from the DHP. Four categories of motion were tested: simple motion (linear translation), cardiac-like motion (normal cardiac cycle), arrhythmia-based motion (irregular heartbeats), and complex arrhythmia-based motion (arrhythmias combined with twisting or torsion). These categories encompassed varying physiological complexities. This was achieved by modulating input signal amplitudes in the VSA software to adjust cardiac rate, heart rate variability, and quiescent period duration (Fig. 2).

Details of these experiments are summarized in Table I and further elaborated in Fig. A2 of the Appendix. As reported in table 1, Arrhythmia-based motions required longer window lengths than cardiac-like ECG motion (Group 2) due to increased variability and complexity. Arrhythmic patterns, characterized by irregular cycle timing, necessitated extended windows to ensure accurate quiescent period detection. The Quiescent Period Length (QPL), defined as low-motion duration, was longer in arrhythmia-based groups (1–3 cycles)

TABLE I
EXPERIMENT DETAILS FOR ALGORITHM PERFORMANCE EVALUATION WITH
VARIOUS MOTION TYPES ON THE DHP

	GROUP 1 (SIMPLE MOTION)	GROUP 2 (CARDIAC -LIKE ECG MOTION)	GROUP 3 (CARDIAC- LIKE ARRHYTHMIA- BASED MOTION)	GROUP 4 (ARRHYTHMIA -BASED COMPLEX MOTION)
WINDOW LENGTH (WL)	100-200 MS	50-150 MS	50-200 MS	50-200 MS
WINDOW CENTER (WC)	400-700 MS	400-700 MS	400-700 MS	400-850 MS
QUIESCENT PERIOD LENGTH (QPL)	1 TO 2	1 TO 2	1 TO 3	1 TO 3

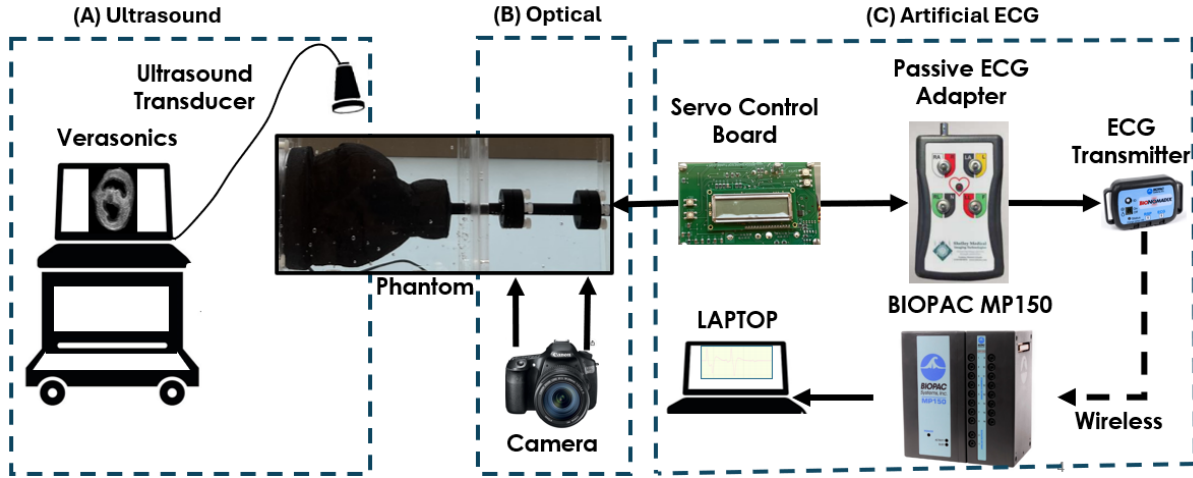


Fig. 3. Trimodal data acquisition experimental setup used to acquire echocardiography, passive ECG and optical images asynchronously for the same motion sequence produced by the DHP. (A) The US data is acquired using a P4-1 Phillips transducer, and a Verasonics Vantage hardware system. (B) The control board drives the two servo-motors of the DHP, corresponding to linear and torsional motion, producing cardiac-like motion. A Canon EOS 60D camera is utilized to acquire optical images of the DHP extender arm, providing extensive information about phantom movement that is used as the ground truth for its motion. (C) The passive ECG adapter further processes the signals from the control board. The BIOPAC acquisition module then transfers the resulting passive ECG signal to the laptop.

compared to Group 2 (1–2 cycles), facilitating robust analysis and noise reduction. Preprocessing techniques were then applied to reduce noise, boost signal clarity, and extract key features for each signal modality, as detailed in the following subsections.

i. Optical Data

First, 60 Hz videos were converted to grayscale, followed by resizing the frames to a dimension of 1080 by 720, ensuring consistency across the dataset. Intensity values were normalized to standardize lighting and contrast, reducing bias. Spatial noise was reduced using a bilateral filter, preserving edges while minimizing noise, with parameters optimized to maintain anatomical detail. A template tracking technique was applied using a 15×15 -pixel search window to precisely track the region of interest, defined as the phantom's driving axis [27]. Velocity was derived by measuring template displacement across frames and dividing by the frame interval, yielding values in mm/s. The DHP's physical dimensions were used for calibration, forming the ground truth for the US-ECG

fusion prediction algorithm.

ii. Artificial ECG Signal

Similarly, passive ECG signals produced by the DHP with a sampling rate of 60 Hz were segmented based on detected R-peaks, which represent the point of maximum upward deflection during each cardiac cycle. The ECG signal was first filtered to reduce noise using a 4th-order Butterworth low-pass filter with a cutoff frequency of 30 Hz, implemented in MATLAB [28]. Next, the Pan-Tompkins algorithm [29] is utilized to detect the R-peaks using a combination of differentiation, squaring, and integration to improve peak detection. Once R peaks are detected, the ECG signal is segmented into individual beats. Each segment typically starts at one R peak and ends just before the next R peak, ensuring that each segment represents one complete cardiac cycle.

To improve the physiological realism of passive ECG signals, the addition of noise and an augmentation pipeline was applied prior to model training. This included adaptive smoothing of QRS complexes and insertion of synthetic P-

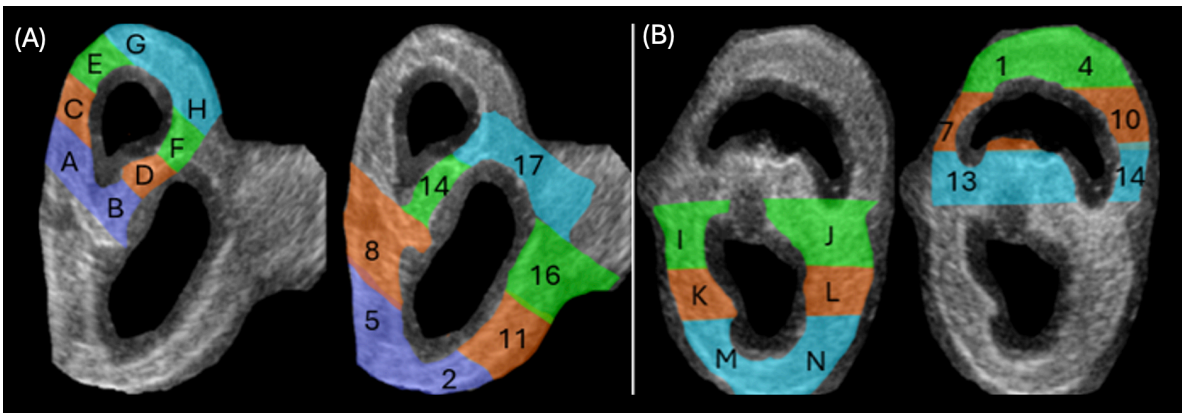


Fig. 4. Segmentation model of PS�A and PSSA views of the US cardiac phantom data. The color-coded regions correspond to different anatomical sections. Each region is labeled alphabetically (A-N) for PS�A (A) and numerically (1-17) for PSSA (B), facilitating precise tracking of specific areas across cardiac cycles.

waves using a Gaussian window preceding each detected R-peak. Controlled noise components like Gaussian noise, baseline wander, and powerline interference were introduced, and the signal-to-noise ratio was adjusted to approximately 15–20 dB to match clinical ECG characteristics. Additional augmentations such as time stretching, amplitude scaling, and temporal shifting were implemented to simulate inter-subject variability. The modified ECG signals were then compared to real ECG cycles using Pearson correlation coefficients, which ranged from 0.46 to 0.87 depending on heart rate and morphology. These modified passive ECG signals were subsequently used as input to the 3D CNN–ANN framework for quiescent phase prediction, enabling performance comparisons between original and modified inputs.

iii. Ultrasound Videos

Ultrasound frames with a resolution of 512×512 pixels (grayscale, 16-bit) and a frame rate of 60 Hz underwent dynamic range adjustment, noise removal, and manual segmentation, as described below, to enable quantitative analysis of cardiac motion parameters. Dynamic range adjustment stretched intensity values to the full 0–255 range, enhancing contrast and differentiation between structures.

To address speckle noise, adaptive filtering was implemented wherein the frames were first divided into overlapping windows of size 10 by 10 pixels [30]. The mean and variance of the signal within each window were calculated to design an adaptive filter, which dynamically adjusted its parameters, such as cutoff frequency and gain based on amplitude variations and noise levels, to effectively suppress noise. To optimize computational efficiency while maintaining relevant spatial features, ultrasound frames were down-sampled from 512×512 pixels to 96×96 pixels using bilinear

interpolation. The temporal resolution, 60 Hz, was preserved to capture cardiac motion dynamics and pixel intensities were normalized to the range [0, 1].

Finally, manual segmentation was implemented using masks derived from each of the experimental groups in the PSSA and PSIA views via thresholding, Canny edge detection [31] and contour smoothing [32]. It is important to note that in the future the choice of segmentation approach may vary in a clinical setting depending on factors such as the complexity of the structures of interest, the quality of the ultrasound images, individual patient anatomy, and the specific requirements of the application.

B. Validation of DHP movements

To establish correlation between the movements of the entire heart in the DHP and the IVS, velocities were computed using three methods: the Horn-Schunck optical flow method ($\lambda=0.1$, 100 iterations, speckle noise adjustment) [33], particle image velocimetry (32×32 -pixel interrogation window, 16-pixel grid spacing) [34], and a correlation-based phase-to-phase deviation measure (correlation threshold 0.8) [18]. Left and right ventricle segmentation was performed using semi-automated annotation to define region boundaries. Segmentation began with automatic identification of regions of interest across frames, verified via block matching-based template tracking on manually annotated images. Active contours were then applied to track the left and right phantom ventricles over the cardiac cycle [35], with parameters controlling elasticity ($\alpha=0.15$), stiffness ($\beta=0.4$), and a balloon force ($\gamma=0.15$). Gaussian smoothing ($\sigma=1.5$) stabilized gradient calculations, and optimization continued until a convergence tolerance of 10^{-4} was achieved.

Finally, post-processing steps were performed to refine the

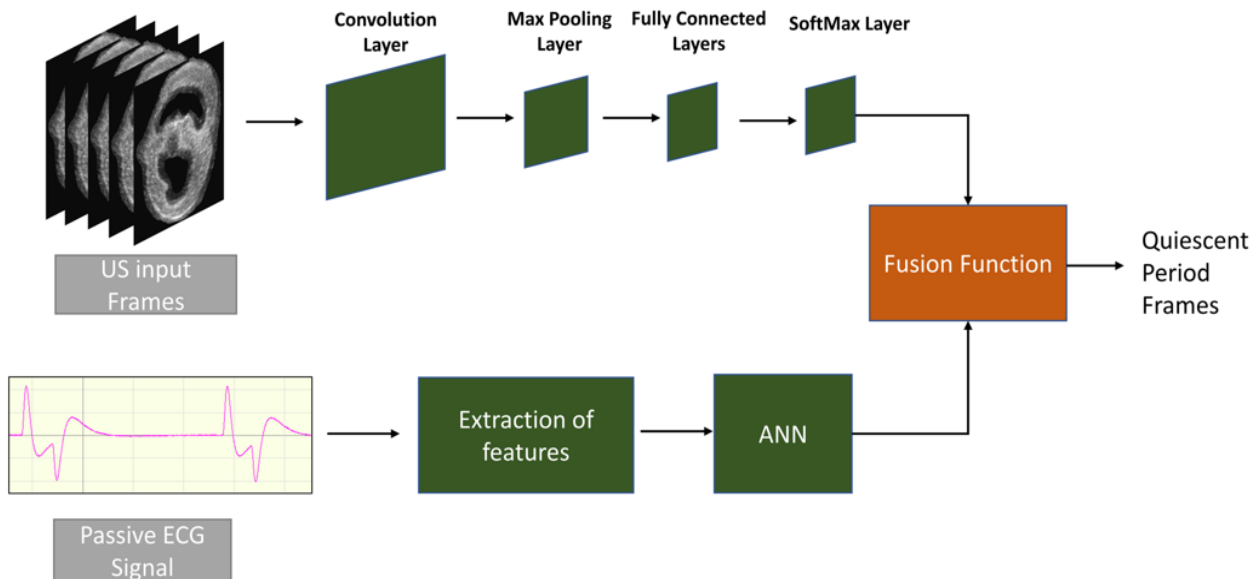


Fig. 5. Deep-learning-based cardiac gating framework. The upper branch uses a 3D CNN to process US images and predict QPs. The lower branch utilizes extracted ECG features, which are input into an ANN to predict quiescence. The outputs of the two branches are fused to give the frames corresponding to the QPs.

segmented ventricular contours and improve segmentation accuracy. While the segmentation process was based on the standardized myocardial segmentation and nomenclature guidelines outlined by the American Heart Association (AHA) [36], modifications were made to ensure the approach aligns with the specific geometry and structure of the phantom. A total of 15 segments were defined across the PSIA and PSSA views to suit the phantom design, as illustrated in Fig. 4. These modifications ensured accurate segmentation while maintaining consistency with the myocardial analysis.

Appendix Figures A6-A8 detail the results from the comparisons of velocity vectors derived from optical videos, artificial ECG signals, and ultrasound (US) frames. The Appendix also includes quantitative accuracy metrics and an analysis of velocity differences across various segments of the cardiac phantom.

C. Deep Learning Prediction Framework

The deep-learning framework consists of 2 branches, the US-based branch and the ECG-based branch (Fig. 5). The US-based processing branch utilized a 3D convolutional neural network (CNN) architecture for classifying US frames corresponding to quiescent periods, while the ECG-based processing branch employed an artificial neural network (ANN) approach to extract features from passive ECG signals indicative of cardiac quiescence. While these prediction architectures have been utilized independently in the literature [37-39], to the best of our knowledge, a combined fusion approach for the purpose of cardiac quiescence prediction using US and ECG data has not been utilized. The choice of a 3D CNN is appropriate for processing US video data, as it can capture both spatial and temporal dimensions [37]. The combination of layers used in this framework allows for feature extraction at various levels of abstraction, subsampling, and normalization to improve training dynamics [40].

The input to the 3D CNN branch consists of ultrasound video data with a shape of (batch size, 60, 96, 96, 1), representing 60 grayscale frames (96×96 pixels each) at a frame rate of 60 Hz, capturing spatial and temporal cardiac motion dynamics. The 3D CNN architecture contains 5 convolution layers, 4 max-pooling 3D layers, 4 batch normalization layers, and 1 dense layer, with the parameters elaborated in Appendix Table A1. This architecture, comprising five Conv3D layers with progressively increasing filters (64, 64, 128, 128, and 256), interleaved with four MaxPooling3D layers and batch normalization for stability, was determined to be optimal for quiescence period accuracy. The ReLU activation functions are used in the convolution layers because they help with the vanishing gradient problem, allowing faster performance and better learning [41]. The Adam optimizer, used with a learning rate of 10^{-6} , is known for its efficiency in handling sparse gradients and adaptive learning rate capabilities [42]. The binary cross-entropy loss function is used as the loss function, as it is standard for binary classification tasks. It measures the performance of a classification model whose output is a probability value between 0 and 1 for each frame of the video. The output of

this branch provides a quiescent period probability for each frame of the video, with a value between 0 and 1 representing the likelihood of the frame belonging to the quiescent period class.

The second branch of the deep-learning framework employs an ANN-based approach, using features extracted from the passive ECG signal as inputs. Selected features included heart rate (HR), heart rate variability (HRV), and a 5th-order autoregressive coefficient, as established in prior work [24] are used as input to the architecture. The ANN comprises a three-layer feed-forward architecture with hyperbolic tangent-sigmoid and log-sigmoid activation functions in the hidden layers, and a softmax activation function in the output layer for multi-class classification. Each frame of the ECG signal is assigned a probability of achieving quiescence. These activation functions effectively capture non-linear patterns in the data.

Outputs from the 3D CNN and ANN branches are fused using a weighted voting mechanism to improve the robustness and reliability of quiescent period predictions. The fusion architecture dynamically adjusts weights based on each branch's precision and recall, initially set at 0.6 for the CNN and 0.4 for the ANN. A conservative voting scheme assigns 'Quiescent Period' to a frame only when both branches agree within a predefined confidence threshold, defaulting to 'Not Quiescent Period' in cases of significant discrepancies or low confidence. This adaptive approach maintains accuracy and reliability while minimizing computational complexity.

D. Deep Learning Framework Implementation

The framework was implemented in Python using the Pytorch library. The training and testing were performed on a MacBook equipped with an Apple M3 chip and 16 GB of unified memory (Apple Inc., Cupertino, California, USA). The full dataset consisted of 1500 cardiac cycles, of which 70% (1050 cycles) were used for training, 15% (225 cycles) for validation, and 15% (225 cycles) for testing. The 3D CNN was trained with a batch size of 4 to balance memory requirements and computational efficiency.

The model was trained for 10 epochs with early stopping, which stopped training if the validation loss did not improve by at least 0.01 over two consecutive epochs. The validation set was used to monitor loss and guide early stopping to prevent overfitting. The implementation was developed using an Adam optimizer. The average training time was approximately 9 hours. Inference was performed on the same machine and required approximately 3 minutes per cardiac cycle, depending on input size.

Partial cardiac cycle segments (i.e. the first 30%, 40%, 50%, 60%, 70% or 80% of US and ECG data from each cycle) were used as input to the deep-learning framework to test the model's ability to predict the QPs within the same cardiac cycle before the occurrence of cardiac quiescence. This design allows for an evaluation of the framework's performance in scenarios requiring early QP identification. For example, the inputs to one of the trained models are only the first 30 frames of the US-based cardiac cycle, instead of the entirety of the cardiac cycle.

TABLE II
ACCURACY OF PREDICTING QP FRAMES IN A CARDIAC CYCLE OF 60 BPM USING THE IVS AND WHOLE PHANTOM (WP) FOR PARTIAL DATASETS

		30%		50%		70%		80%	
SIGNAL TYPE		IVS	WP	IVS	WP	IVS	WP	IVS	WP
ECG GATING	ECG (ORIGINAL)	45.31%		58.64%		83.78%		85.56%	
ANN BRANCH	ECG (ORIGINAL)	54.87%		65.68%		92.85%		93.46%	
	ECG (MODIFIED)	52.46%		58.12%		81.45%		87.23%	
3D CNN BRANCH	US	52.14%	51.92%	69.12%	66.72%	89.14%	92.98%	95.21%	95.18%
3D CNN-ANN FRAMEWORK	US + ECG (ORIGINAL)	61.82 %	58.21 %	75.46%	71.11%	94.47%	95.85%	96.15%	96.59%
	US + ECG (MODIFIED)	60.38%	57.66%	76.91%	69.54%	92.31%	92.67%	96.87%	94.41%

TABLE III
ACCURACY OF PREDICTING QP FRAMES USING THE 50% AND 80% PARTIAL DATASETS FOR BOTH THE WHOLE PHANTOM (WP) AND IVS ONLY.

100 MS < QP < 200 MS			50 MS < QP < 100 MS	
CARDIAC CYCLE %	50%	80%	50%	80%
WHOLE PHANTOM	85.46%	96.23%	72.31%	91.67%
IVS	86.15%	94.9%	71.47%	87.93%

The framework was trained based on the IVS dataset as well as the entire phantom dataset. The number of input frames varied across experiments (e.g., 30% to 80% of a 60-frame cardiac cycle) to simulate different data availability conditions. To ensure compatibility with the fixed 3D CNN architecture, we applied temporal padding for shorter sequences by repeating the final frame to reach the expected input depth. In some cases, reduced-frame inputs were also processed directly by the model without requiring changes to the architecture, as the network was designed to accommodate variable temporal depths up to its effective receptive field.

III. RESULTS

The following section focuses on evaluating the accuracy and reliability of each algorithm using the cardiac phantom. The deep learning-based US-ECG gating framework predicted cardiac QPs within the DHP. Across multiple experiments, the framework identified QP frames using both US and ECG data inputs. The prediction performance for the whole phantom and the interventricular septum (IVS) is reported in Table II across different data availability levels. The results include a standard ECG gating algorithm [32], the ECG-based ANN branch using both original and modified artificial ECG inputs (ECG (Original), ECG (Modified)), the US-based 3D CNN branch (US), and the combined multimodal 3D CNN-ANN framework (US + ECG (Original), US + ECG (Modified)). Modified artificial ECG inputs incorporate P-wave insertion, QRS smoothing, and noise augmentation to better approximate physiological signal characteristics.

TABLE IV
PREDICTION ACCURACY OF CARDIAC GATING ALGORITHMS FOR DIFFERENT CARDIAC WALL REGIONS (WALL 1, WALL 2, WALL 3, WALL 4), THE IVS, AND THE WHOLE PHANTOM, USING PARTIAL DATASETS OF 70% AND 80% OF THE DATA.

	WALL 1		WALL 2		WALL 3	
	70%	80%	70%	80%	70%	80%
ECG GATING	83.78%	85.56%	83.78%	85.56%	83.78%	85.56%
ONLY ECG ANN	90.14%	93.33%	88.67%	90.46%	91.23%	94.24%
ONLY US 3D CNN	90.66%	94.61%	89.23%	92.55%	92.98%	95.18%
US-ECG 3D CNN-ANN	92.16%	95.59%	90.77%	93.19%	95.85%	97.59%
	WALL 4		IVS		WHOLE PHANTOM	
	70%	80%	70%	80%	70%	80%
ECG GATING	83.78%	85.56%	83.78%	85.56%	83.78%	85.56%
ONLY ECG ANN	89.56%	92.74%	90.89%	93.45%	92.85%	93.41%
ONLY US 3D CNN	90.34%	93.62%	91.73%	93.71%	91.14%	95.21%
US-ECG 3D CNN-ANN	91.46%	93.97%	92.38%	94.98%	94.47%	97.15%

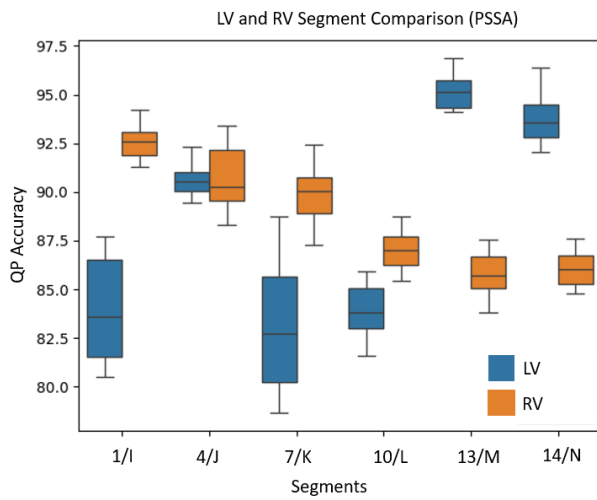


Figure 6: Predicted QP accuracy for segmented left (LV) and right ventricles (RV) for all data acquired using the PSSA view. Segment labels (numbers and letters) are shown in Fig. 4.

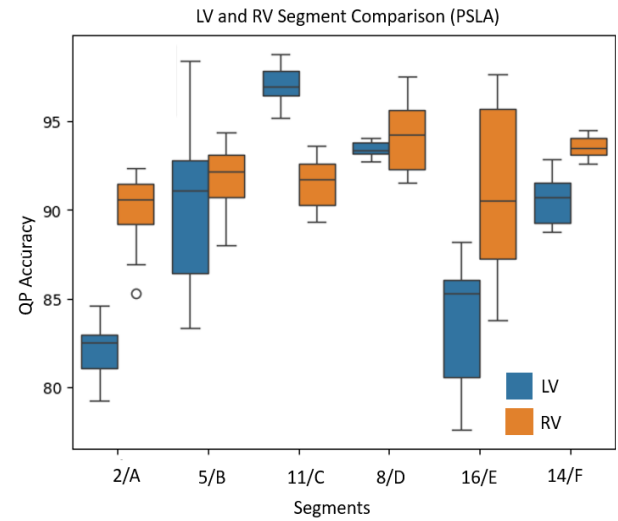


Figure 7: Predicted QP accuracy for segmented left (LV) and right ventricles (RV) for all data acquired using the PSLA view. Segment labels (numbers and letters) are shown in Fig. 4.

The US-ECG 3D CNN-ANN fusion framework consistently has the highest accuracy cross both IVS and whole phantom, from 58.21% accuracy with 30% of the data to 96.87% with 80%. ECG gating has the lowest accuracy. Accuracies are higher for the IVS only compared to the whole phantom. To evaluate the impact of the modified artificial ECG signal, QP prediction accuracy was compared between original and modified artificial ECG signals across both the IVS and the whole phantom. In the ECG-only ANN branch, the modified ECG yielded slightly lower or comparable

accuracy relative to the original ECG across all data availability levels. For instance, at 80% data usage, ECG (Mod) achieved 87.23% accuracy in the WP compared to 93.46% with ECG (Orig). However, within the multimodal US + ECG 3D CNN-ANN framework, modified ECG inputs performed competitively, particularly in the IVS region, where the modified version achieved 96.87% accuracy at 80%, slightly outperforming the original input (96.15%). These results suggest that while modification of artificial ECG signals may not consistently improve only ECG-ANN performance, they can contribute positively to multimodal

TABLE V
COMPARISON OF QP ACROSS ECG SEGMENTS FOR THE WHOLE PHANTOM

EXPERIMENT CATEGORY	METHOD	QRS	ST	TP	PQ	QP1	QP2
SIMPLE LINEAR	ONLY ECG	98.5%	92.2%	87.6%	99.5%	91.2%	88.3%
SIMPLE LINEAR	ONLY US	96.5%	93.4%	97.8%	97.5%	94.4%	96.5%
SIMPLE LINEAR	US-ECG	99.5%	95.3%	98.2%	99.5%	95.3%	98.7%
SIMPLE LINEAR + TORSION	ONLY ECG	97.3%	95.1%	89.8%	99.5%	95.2%	81.3%
SIMPLE LINEAR + TORSION	ONLY US	95.4%	94.7%	96.4%	96.2%	96.6%	95.4%
SIMPLE LINEAR + TORSION	US-ECG	99.3%	97.8%	97.8%	99.5%	98.3%	97.8%
SIMPLE ECG	ONLY ECG	84.5%	89.4%	82.1%	95.4%	83.6%	83.5%
SIMPLE ECG	ONLY CNN	91.6%	90.7%	92.3%	96.5%	87.9%	95.1%
SIMPLE ECG	US-ECG	92.4%	94.3%	93.7%	97.3%	91.1%	94.8%
COMPLEX ECG	ONLY ECG	82.2%	84.5%	81.3%	89.3%	84.3%	85.4%
COMPLEX ECG	ONLY US	91.8%	89.3%	92.6%	88.1%	90.3%	94.4%
COMPLEX ECG	US-ECG	91.8%	91.3%	94.5%	93.3%	93.4%	96.7%

cardiac gating.

Table III presents the prediction accuracies for QPs of different durations (QPs between 100 ms and 200 ms, and QPs between 50 ms and 200 ms) for two dataset sizes (50% and 80% of the cardiac cycle) across the whole phantom dataset and the IVS-specific dataset. For the QP durations between 100 ms and 200 ms, both datasets show higher accuracies when using 80% of the data compared to 50% of the data, with the IVS-only dataset achieving slightly higher accuracies in both data conditions compared to the whole phantom dataset.

Conversely, for the shorter frame duration range (QP durations between 50 ms and 200 ms), the whole phantom dataset performs better, particularly when using 80% of the data where accuracy is 91.67% compared to the IVS only dataset (87.93%). This suggests that while the IVS dataset may be more accurate for longer QP durations, the whole phantom dataset provides better performance for shorter QP frame durations.

Table IV presents the prediction accuracy of various cardiac gating algorithms across different cardiac wall regions (Wall 1, Wall 2, Wall 3, and Wall 4), the IVS and the whole phantom, using 70% and 80% partial datasets. The US-ECG 3D CNN-ANN framework outperformed other methods in all cases, achieving the highest prediction accuracy, such as 97.59% for Wall 3 and 97.15% for the whole phantom dataset at 80% data usage. The Only US 3D CNN framework also performed strongly, with accuracies slightly below those of the fused framework, such as 95.18% for Wall 3 and 95.21% for the whole phantom dataset at 80% data usage. In contrast, the ECG gating algorithm yielded the lowest accuracies, with a maximum accuracy of 85.56% across all walls and datasets. These results demonstrate better accuracy using the fused US-ECG 3D CNN-ANN framework compared to individual frameworks and traditional ECG gating.

The accuracy of predicting quiescent periods (QPs) is shown in Fig. 6 for the PSSA view for the segments shown previously in Fig. 4. In the left ventricle, segments 13 and 14 have the highest prediction accuracy, while in the right ventricle, segments I and J are associated with the highest prediction accuracy. Similarly, in the PSLA view in Fig. 7, segments 8 and 11 in the left ventricle and segments C and D in the right ventricle have the highest predicted QP accuracy.

Finally, a comparative analysis of the predictive algorithm across various cardiac cycle segments, using the passive ECG signal as a marker, is provided in Table V for the whole phantom. These columns represent the accuracy of detecting QP in specific segments of the cardiac cycle. The highest accuracy in QRS detection was observed with the US-ECG combination under the 'Simple Linear' experiment group, scoring 99.5%. However, a notable difference is found in the TP segment, i.e., the segment between the T and P waves of the ECG, wherein the US-ECG framework outperforms the Only ECG model. The US-ECG framework shows better performance across several cases, particularly for TP and PQ detection, achieving accuracies over 92%. For the ST segment, the best result comes from the Simple Linear + Torsion experiment group, with the US-ECG framework achieving

97.8% accuracy.

IV. DISCUSSION

Improving cardiac QP prediction and maintaining high diagnostic accuracy are critical for enhancing CTA reliability and outcomes in challenging patient populations [44,45]. Across multiple experiments, the framework predicted cardiac quiescence accuracies in identifying frames corresponding to QPs, leveraging both US and ECG data inputs. Notably, the framework's predictive capabilities achieved accuracies exceeding 90% in some cases across both the whole and IVS datasets. These results underscore the potential of deep learning algorithms to effectively predict cardiac motion in clinical imaging settings. Analysis of the framework's performance revealed notable differences in prediction accuracy between experiments utilizing the entire phantom dataset and those focusing solely on the IVS. Experiments utilizing the entire phantom dataset yielded slightly higher accuracy rates. However, similar performance in experiments when only the IVS was used emphasizes the potential for streamlining gating algorithms, reducing computational complexity, and optimizing resource utilization in real-world clinical scenarios [43].

CTA achieves high diagnostic accuracy (sensitivity 85–99%, specificity 64–92%) for CAD detection. Importantly, motion artifacts and non-diagnostic scans remain challenges in arrhythmic patients [46,47,48]. Robust algorithms maintaining accuracy with partial or incomplete data are critical for reducing non-diagnostic scans and enhancing reliability in noisy instances [47]. Incomplete datasets in medical imaging significantly reduce diagnostic accuracy, as studies show compromised performance in machine learning models for cardiac disease diagnosis and reduced accuracy in brain tumor segmentation when data is missing. These findings highlight the importance of comprehensive data to ensure reliable diagnostics and precise medical imaging analysis [49].

The predictive accuracy across various partial datasets consistently improves when an increasing percentage of the cardiac cycle is included in the dataset. This trend was observed across all algorithms, with the US-ECG 3D CNN-ANN method consistently outperforming other approaches. For example, the US-ECG 3D CNN-ANN method's accuracy increased from 58.21% with 30% of the dataset to 96.59% when using 80%, particularly when applied to the IVS dataset. This demonstrates the significant advantage of high-resolution, integrated data techniques in improving diagnostic accuracy for localized cardiac regions such as the IVS, which plays a crucial role in tracking of cardiac motion.

This work also highlights notable differences in accuracy between the IVS and whole phantom datasets across different QP intervals, particularly in the 50 ms to 100 ms QP range, which poses a greater challenge due to the increased complexity of cardiac motion during shorter quiescent phases. Despite the dynamic nature of the IVS, the advanced methodologies employed, particularly the US-ECG 3D CNN-ANN method, were able to maintain robust performance, especially in the 80% dataset range where accuracy approached 88%. This indicates that although the IVS presents

more variability, it remains a strong candidate for predictive accuracy, potentially offering a streamlined approach for real-world applications in gating cardiac CTA.

The results also reveal regional variability across different cardiac segments, with certain regions, such as the IVS, showing superior predictive accuracy, especially when using more sophisticated algorithms like the US-ECG 3D CNN-ANN method. The US-ECG method showed an 11 percent improvement in quiescent phase prediction accuracy over ECG-only gating in the IVS. While promising, the clinical impact remains to be validated. Prior studies have shown that a 5 to 10 percent phase difference can significantly affect diagnostic quality, particularly for motion-sensitive vessels like the right coronary artery [50] and may reduce diagnostic yield by up to 66 percent in certain cases [51]. Future reader studies using phantom and human datasets will be essential to assess the diagnostic value of US-ECG-guided gating. In contrast, other regions, such as Wall 4, exhibit slightly lower accuracy rates, potentially due to their anatomical and functional complexity. These findings suggest that region-specific imaging strategies could improve diagnostic accuracy, further supporting the need for tailored approaches rather than a one-size-fits-all solution in cardiac imaging.

To overcome the possible limitation of the simple artificial ECG signals used with the phantom, additional noise was introduced, and an augmentation pipeline produced waveforms with improved morphological fidelity to produce ECG (Mod). P-wave synthesis, QRS smoothing, and the addition of clinically relevant noise contributed to closer alignment with real ECG characteristics (Appendix, Figures A3, A4, A5) [52]. Quantitative comparisons showed a moderate to strong correlation with real ECG data, and the use of the modified signals in the 3D CNN-ANN framework resulted in comparable quiescent phase prediction. These observations highlight the importance of signal quality in model performance. Nevertheless, artificial ECGs remain a simplified, albeit idealized, representation of cardiac signals. With these highly idealized signals, our ability to detect cardiac quiescence is limited without the US information, because analyzing noisier signals using ECG-alone will lead to less optimal predictions of gating intervals in the phantom. Nevertheless, further validation using real-time clinical ECG data is necessary to confirm generalizability in clinical settings.

To evaluate the clinical relevance of multimodal gating, we present a case-wise comparison (Appendix, Table A2, Table A3) illustrating the performance of ECG-only, modified ECG, and US-based quiescent phase predictions. While average improvements in accuracy were modest, the examples demonstrate that multimodal input improved robustness in scenarios with arrhythmias or short-duration QPs. Notably, modified ECG signals showed benefits in capturing P-wave adjacent quiescent phases, whereas US outperformed ECG in detecting brief or fragmented motion patterns. These trends underscore the value of incorporating complementary modalities to optimize gating consistency in challenging cardiac conditions.

While ECG gating achieved 85.56% accuracy in the whole phantom dataset at 80% data usage, the US-ECG 3D CNN-ANN method consistently exceeded this, demonstrating its

flexibility across diverse cardiac segments and challenging conditions like arrhythmias. The addition of ultrasound data provides unique value as it captures 2D spatial variations of the heart, offering insights into cardiac motion and structural dynamics that are not accessible through ECG, which is limited to the electrical characterization of the heart without spatial information. The performance variability across cardiac walls highlights the importance of region-specific imaging protocols to optimize accuracy and efficiency.

The chief limitation of this study is that it relies on phantom data; thus the performance of the fused US-ECG CNN-ANN techniques may not translate readily to diverse patient settings. While the DHP used in this study incorporates variability in heart rate, including experiments involving arrhythmia-based conditions, it remains a simplified model that does not fully replicate the complexity of in vivo cardiac motion. The phantom lacks key physiological characteristics such as tissue heterogeneity, blood flow dynamics, and myocardial deformation, which are critical for modeling realistic cardiac behavior. As a result, while the experiments include controlled variations in heart rate and rhythm, they do not fully reflect the diversity of pathological conditions and structural abnormalities encountered in clinical practice.

Additionally, the focus on phantom datasets, including incomplete (partial) and IVS-specific data, may introduce biases and limit the generalizability of the framework's performance to real-world cases. Future segmentation strategies will be guided by the clinical objective, imaging conditions, and target vessel. For cardiac gating, segmentation may focus on the IVS, which is a reliable indicator of quiescent periods. However, the optimal region for segmentation may vary depending on the vessel of interest. For example, the right coronary artery may exhibit different quiescent timing than the left main or anterior descending arteries. Broader assessments, such as global contractility or wall motion abnormalities, may require endocardial and epicardial boundaries. The optimal myocardial region may also vary by vessel, such as the quiescent phase suitable for the RCA, which may differ from that of the LM or LAD. In repeat CTA cases, prior motion artifacts could guide region-specific segmentation to improve gating accuracy. In complex imaging scenarios, fiducial markers can assist with landmark detection while allowing for clinician input in low-confidence regions. These developments balance segmentation accuracy with clinical adaptability and support progress towards real-time decision-making across diverse cardiac imaging applications.

The reliance on both US and ECG data poses practical challenges in clinical settings, where signal quality can be affected by operator variability, noise, or imaging artifacts such as speckle noise and shadowing. To support clinical translation, we plan to transition from phantom-based training to real human imaging through a staged adaptation pipeline. As an initial step, the trained model will be evaluated on retrospective human ultrasound datasets such as CAMUS [53], which offers annotated echocardiographic videos suitable for assessing segmentation and motion alignment. These evaluations will inform fine-tuning through transfer learning techniques, including weight freezing and domain adaptation strategies such as adversarial training. Additionally, future

iterations will incorporate a CT-compatible ultrasound transducer to collect in vivo cardiac data under clinically relevant conditions, enabling model adaptation to real-world variability in anatomy, signal quality, and acquisition protocols.

Additionally, the computational demands of the framework may limit its integration into real-time workflows, requiring further optimization. Although the current model is not optimized for real-time inference, the average prediction time of ~ 3 minutes per cardiac cycle suggests potential for integration into semi-automated workflows. Future iterations will explore complexity reduction strategies such as model quantization, pruning, and hardware acceleration to improve speed and efficiency. Notably, the framework supports variable-length input sequences, allowing a reduced number of frames to be processed without requiring changes to the underlying architecture. This adaptability may offer additional advantages in time-constrained clinical settings where shorter acquisitions are preferred. While direct comparisons to clinical gating speeds are not yet available, improving inference efficiency remains a priority to support integration into time-sensitive imaging workflows. The ultimate impact of improved gating on coronary CTA diagnostic accuracy also needs to be assessed. Addressing these limitations is essential to strengthen robustness and enable clinical applications in the future.

V. CONCLUSION

This study presents a novel approach to CTA gating through the integration of phantom-derived cardiac data and a deep learning framework. A key strength of the work is the development of a flexible fusion architecture that integrates US and ECG data, supporting robust detection of cardiac quiescent periods across diverse motion patterns and anatomical regions. The system is designed for adaptability, offering a practical foundation for incorporating advanced imaging and prediction techniques into clinical workflows. The use of a dynamic heart motion phantom ensures a controlled evaluation environment, bridging the gap between experimental validation and clinical translation. By combining US and ECG data, the proposed US-ECG deep learning framework provides a solution for accurately predicting cardiac quiescent periods, with demonstrated potential for clinical applications based on its performance across phantom datasets and effective handling of the structurally complex regions such as the IVS. Our findings suggest that multimodal deep learning frameworks can potentially improve diagnostic quality and reliability in challenging patient populations, particularly those with high or irregular heart rates where even small gating errors can result in nondiagnostic scans. This supports the potential for improved CTA gating and broader applications in cardiac imaging.

APPENDIX

The Appendix provides figures and tables supporting the detailed validation process. This section includes substantial supplementary information to facilitate the understanding of the methods and results discussed in the main text.

ACKNOWLEDGMENT

The authors thank Sunny Kim, Stephan Strassle Rojas, and Bowen Jing at the Georgia Institute of Technology for their assistance with the experimental setup.

REFERENCES

- [1] World Health Organization, "Cardiovascular disease statistics," available at: https://www.who.int/health-topics/cardiovascular-diseases#tab=tab_1, accessed Mar. 21, 2024.
- [2] J. D. Berry *et al.*, "Lifetime risks of cardiovascular disease," *New England Journal of Medicine*, vol. 366, no. 4, pp. 321–329, 2012.
- [3] D. S. Desai and S. Hajouli, "Arrhythmias," in *StatPearls [Internet]*, StatPearls Publishing, 2022.
- [4] American Heart Association, "2022 heart and stroke statistical update: Global burden of disease," available at: <https://www.heart.org/-/media/PHD-Files-2/Science-News/2/2022-Heart-and-Stroke-Stat-Update/2022-Stat-Update-factsheet-Global-Burden-of-Disease.pdf>, accessed Dec. 19, 2024.
- [5] E. Michniewicz *et al.*, "Patients with atrial fibrillation and coronary artery disease – Double trouble," *Advances in Medical Sciences*, vol. 63, no. 1, pp. 30–35, 2018, DOI: [10.1016/j.advms.2017.06.005](https://doi.org/10.1016/j.advms.2017.06.005).
- [6] M. Abubakar *et al.*, "Advancements in percutaneous coronary intervention techniques: A comprehensive literature review of mixed studies and practice guidelines," *Cureus*, vol. 15, no. 7, p. e41311, Jul. 2023, DOI: [10.7759/cureus.41311](https://doi.org/10.7759/cureus.41311).
- [7] M. G. Bourassa, "The history of cardiac catheterization," *The Canadian Journal of Cardiology*, vol. 21, no. 12, pp. 1011–1014, 2005.
- [8] M. Tavakol, S. Ashraf, and S. J. Brenner, "Risks and complications of coronary angiography: A comprehensive review," *Global Journal of Health Science*, vol. 4, no. 1, p. 65, 2012.
- [9] P. Ganz *et al.*, "Association of osteopontin, neopterin, and myeloperoxidase with stroke risk in patients with prior stroke or transient ischemic attacks: Results of an analysis of 13 biomarkers from the stroke prevention by aggressive reduction in cholesterol levels trial," *Stroke*, vol. 48, no. 12, pp. 3223–3231, 2017.
- [10] L. P. Dawson *et al.*, "Care models for acute chest pain that improve outcomes and efficiency: JACC state-of-the-art review," *Journal of the American College of Cardiology*, vol. 79, pp. 2333–2348, Jun. 14, 2022.
- [11] A. Schmermund *et al.*, "Declining radiation dose of coronary computed tomography angiography: German cardiac ct registry experience 2009–2014," *Clinical Research in Cardiology*, vol. 106, pp. 905–912, 2017.
- [12] M. Gulati *et al.*, "2021 AHA/ACC/AASE/CHEST/SAEM/SCCT/SCMR guideline for the evaluation and diagnosis of chest pain: A report of the American College of Cardiology/American Heart Association Joint Committee on Clinical Practice Guidelines," *Journal of the American College of Cardiology*, vol. 78, pp. e187–e285, Nov. 30, 2021.
- [13] D. C. M. Chan *et al.*, "Selective referral using coronary computed tomography angiography versus direct referral for individuals referred to invasive coronary angiography: The CONSERVE Trial," *Journal of Cardiovascular Computed Tomography*, vol. 15, no. 1, pp. 5–14, 2021, doi: [10.1016/j.jcct.2020.10.009](https://doi.org/10.1016/j.jcct.2020.10.009).
- [14] S. S. Virani *et al.*, "Heart disease and stroke statistics—2020 update: A report from the American Heart Association," *Circulation*, vol. 141, no. 9, pp. e139–e596, 2020.
- [15] B. Desjardins and E. A. Kazerooni, "ECG-gated cardiac CT," *American Journal of Roentgenology*, vol. 182, no. 4, pp. 993–1010, 2004.
- [16] C. Wick *et al.*, "Echocardiography as an indication of continuous-time cardiac quiescence," *Physics in Medicine & Biology*, vol. 61, no. 14, p. 5297, 2016.
- [17] S. Tridandapani *et al.*, "Echocardiography-based selection of quiescent heart phases: Implications for cardiac imaging," *Journal of Ultrasound in Medicine*, vol. 24, no. 11, pp. 1519–1526, 2005.
- [18] C. A. Wick *et al.*, "Detection of cardiac quiescence from B-mode echocardiography using a correlation-based frame-to-frame deviation measure," *IEEE Journal of Translational Engineering in Health and Medicine*, vol. 1, pp. 1 900 211–1 900 211, 2013.
- [19] C. A. Wick *et al.*, "A system for seismocardiography-based identification of quiescent heart phases: Implications for cardiac imaging," *IEEE Transactions on Information Technology in Biomedicine*, vol. 16, no. 5, pp. 869–877, 2012.

- [20] C. A. Wick *et al.*, "Seismocardiography-based detection of cardiac quiescence," *IEEE Transactions on Biomedical Engineering*, vol. 62, no. 8, pp. 2025–2032, Aug. 2015, DOI: [10.1109/TBME.2015.2411155](https://doi.org/10.1109/TBME.2015.2411155).
- [21] B. De Man *et al.*, "Metal streak artifacts in X-ray computed tomography: A simulation study," in *1998 IEEE Nuclear Science Symposium Conference Record. 1998 IEEE Nuclear Science Symposium and Medical Imaging Conference (Cat. No. 98CH36255)*, vol. 3, pp. 1860–1865, 1998.
- [22] S. S. Rojas *et al.*, "A thin transducer with integrated acoustic metamaterial for cardiac CT imaging and gating," *IEEE Transactions on Ultrasonics, Ferroelectrics, and Frequency Control*, vol. 69, no. 3, pp. 1064–1076, 2021.
- [23] S. S. Rojas *et al.*, "Ultrasound-gated computed tomography coronary angiography (CTCA): Development of ultrasound transducers with improved CT compatibility," *Medical Physics*, Jun. 4, 2021.
- [24] J. Yao *et al.*, "An adaptive seismocardiography (SCG)-ECG multimodal framework for cardiac gating using artificial neural networks," *IEEE Journal of Translational Engineering in Health and Medicine*, vol. 6, pp. 1–11, 2018.
- [25] Shelley Tech, "Dynamic Heart Phantom DHP-01," available at: <http://www.simutec.com/Docs/Dynamic%20Multi-modality%20Heart%20Phantom%20LR.pdf>, accessed Mar. 21, 2024.
- [26] R. M. Lang *et al.*, "Recommendations for cardiac chamber quantification by echocardiography in adults: An update from the American Society of Echocardiography and the European Association of Cardiovascular Imaging," *Journal of the American Society of Echocardiography*, vol. 28, no. 1, pp. 1–39, 2015, DOI: [10.1016/j.echo.2014.10.003](https://doi.org/10.1016/j.echo.2014.10.003).
- [27] A. Yilmaz *et al.*, "Object tracking: A survey," *ACM Computing Surveys*, vol. 38, no. 4, pp. 1–45, Dec. 2006, DOI: [10.1145/1177352.1177355](https://doi.org/10.1145/1177352.1177355).
- [28] S. Butterworth, "On the theory of filter amplifiers," *Wireless Engineer*, vol. 7, no. 6, pp. 536–541, 1930.
- [29] J. Pan and W. J. Tompkins, "A real-time QRS detection algorithm," *IEEE Transactions on Biomedical Engineering*, vol. BME-32, no. 3, pp. 230–236, Mar. 1985.
- [30] J. Arenas-Garcia *et al.*, "Combinations of adaptive filters," *IEEE Signal Processing Magazine*, vol. 33, no. 1, pp. 120–140, Jan. 2016, DOI: [10.1109/MSP.2015.2474395](https://doi.org/10.1109/MSP.2015.2474395).
- [31] Y. Dong and S. Wang, "An improved Canny edge detection algorithm with iteration gradient," *IEEE Transactions on Image Processing*, DOI: [10.1109/TIP.2023.10040523](https://doi.org/10.1109/TIP.2023.10040523), 2023.
- [32] M. Unser *et al.*, "B-spline signal processing: Part I—Theory," *IEEE Transactions on Signal Processing*, vol. 41, no. 2, pp. 821–833, Feb. 1993, DOI: [10.1109/78.193220](https://doi.org/10.1109/78.193220).
- [33] B. K. P. Horn and B. G. Schunck, "Determining optical flow," *Artificial Intelligence*, vol. 17, no. 1–3, pp. 185–203, Aug. 1981, DOI: [10.1016/0004-3702\(81\)90024-2](https://doi.org/10.1016/0004-3702(81)90024-2).
- [34] R. J. Adrian, "Twenty years of particle image velocimetry," *Experiments in Fluids*, vol. 39, no. 2, pp. 159–169, Jul. 2005, DOI: [10.1007/s00348-005-0991-7](https://doi.org/10.1007/s00348-005-0991-7).
- [35] S. Lankton and A. Tannenbaum, "Localizing region-based active contours," *IEEE Transactions on Image Processing*, vol. 17, no. 11, pp. 2029–2039, Nov. 2008, DOI: [10.1109/TIP.2008.2004611](https://doi.org/10.1109/TIP.2008.2004611).
- [36] M. D. Cerqueira *et al.*, "Standardized myocardial segmentation and nomenclature for tomographic imaging of the heart: A statement for healthcare professionals from the Cardiac Imaging Committee of the Council on Clinical Cardiology of the American Heart Association," *Circulation*, vol. 105, no. 4, pp. 539–542, 2002, DOI: [10.1161/hc0402.102975](https://doi.org/10.1161/hc0402.102975).
- [37] A. Fiorito *et al.*, "Detection of cardiac events in echocardiography using 3D convolutional recurrent neural networks," in *2018 IEEE International Ultrasonics Symposium (IUS)*, pp. 1–4, 2018, DOI: [10.1109/IUS.2018.8570763](https://doi.org/10.1109/IUS.2018.8570763).
- [38] H. Yang *et al.*, "Improving catheter segmentation and localization in 3D cardiac ultrasound using direction-fused FCN," in *2019 IEEE 16th International Symposium on Biomedical Imaging (ISBI 2019)*, pp. 1122–1126, 2019, DOI: [10.1109/ISBI.2019.8759193](https://doi.org/10.1109/ISBI.2019.8759193).
- [39] J. Yao *et al.*, "An adaptive seismocardiography (SCG)-ECG multimodal framework for cardiac gating using artificial neural networks," *IEEE Journal of Translational Engineering in Health and Medicine*, vol. 6, pp. 1–11, 2018, DOI: [10.1109/JTEHM.2018.2855944](https://doi.org/10.1109/JTEHM.2018.2855944).
- [40] J. Schmidhuber, "Deep learning in neural networks: An overview," *Neural Networks*, vol. 61, pp. 85–117, 2015, DOI: [10.1016/j.neunet.2014.09.003](https://doi.org/10.1016/j.neunet.2014.09.003).
- [41] V. Nair and G. E. Hinton, "Rectified linear units improve restricted Boltzmann machines," in *Proceedings of the 27th International Conference on Machine Learning (ICML-10)*, pp. 807–814, 2010.
- [42] D. P. Kingma and J. Ba, "Adam: A method for stochastic optimization," *arXiv preprint*, arXiv:1412.6980, 2014.
- [43] M. K. Friedberg and A. N. Redington, "Right versus left ventricular failure: Differences, similarities, and interactions," *Circulation*, vol. 129, no. 9, pp. 1033–1044, 2014, DOI: [10.1161/CIRCULATIONAHA.113.001375](https://doi.org/10.1161/CIRCULATIONAHA.113.001375).
- [44] O. Ghekiere *et al.*, "Image quality in coronary CT angiography: challenges and technical solutions," *British Journal of Radiology*, vol. 90, no. 1072, p. 20160567, Apr. 2017, doi: [10.1259/bjr.20160567](https://doi.org/10.1259/bjr.20160567).
- [45] J. H. Lee *et al.*, "Quantitative assessment of coronary CT angiography image quality with a motion artifact scoring system," *Journal of Digital Imaging*, vol. 27, no. 4, pp. 472–478, Aug. 2014, doi: [10.1007/s10278-014-9702-3](https://doi.org/10.1007/s10278-014-9702-3).
- [46] P. W. Serruys *et al.*, "Coronary computed tomographic angiography for complete assessment of coronary artery disease," *Journal of the American College of Cardiology*, vol. 78, no. 6, pp. 713–736, 2021, DOI: [10.1016/j.jacc.2021.06.019](https://doi.org/10.1016/j.jacc.2021.06.019).
- [47] K. R. Branch *et al.*, "Diagnostic accuracy of early computed tomographic coronary angiography to detect coronary artery disease after out-of-hospital circulatory arrest," *Resuscitation*, vol. 153, pp. 243–250, Aug. 2020, DOI: [10.1016/j.resuscitation.2020.04.033](https://doi.org/10.1016/j.resuscitation.2020.04.033), PMID: 32422241.
- [48] D. I. Feldman *et al.*, "Coronary computed tomography angiography in patients with stable coronary artery disease," *Trends in Cardiovascular Medicine*, vol. 32, no. 7, pp. 421–428, Oct. 2022, DOI: [10.1016/j.tcm.2021.08.009](https://doi.org/10.1016/j.tcm.2021.08.009), PMID: 34454051.
- [49] X. Chen *et al.*, "Cardiac disease diagnosis based on GAN in case of missing data," *PLOS ONE*, Nov. 22, 2024, DOI: [10.1371/journal.pone.0292480](https://doi.org/10.1371/journal.pone.0292480).
- [50] C. A. Wick *et al.*, "Characterization of cardiac quiescence from retrospective cardiac computed tomography using a correlation-based phase-to-phase deviation measure," *Medical Physics*, vol. 42, no. 2, pp. 983–993, Feb. 2015.
- [51] M. A. Dewey *et al.*, "Dual-source computed tomography angiography image quality in patients with fast heart rates," *European Radiology*, vol. 19, pp. 2341–2348, 2009, DOI: [10.1007/s00330-009-1403-4](https://doi.org/10.1007/s00330-009-1403-4).
- [52] G. D. Clifford *et al.*, "Advanced Methods and Tools for ECG Data Analysis," Norwood, MA: Artech House, 2006.
- [53] N. Leclerc *et al.*, "Deep learning for segmentation using an open large-scale dataset in 2D echocardiography," *IEEE Transactions on Medical Imaging*, vol. 38, no. 9, pp. 2198–2210, Sept. 2019.